Earth and Planetary Science Letters 475 (2017) 224–230

Contents lists available at ScienceDirect

Earth and Planetary Science Letters

www.elsevier.com/locate/epsl

Strong near-surface seismic anisotropy of Taiwan revealed by coda interferometry

Li-Wei Chen [a,b], Ying-Nien Chen [c], Yuancheng Gung [a,*], Jian-Cheng Lee [d], Wen-Tzong Liang [d]

[a] Department of Geosciences, National Taiwan University, Taiwan
[b] Department of Earth and Planetary Science, University of California at Berkeley, CA, USA
[c] Institute of Oceanography, National Taiwan University, Taiwan
[d] Institute of Earth Sciences, Academia Sinica, Taipei, Taiwan

ARTICLE INFO

Article history:
Received 10 March 2017
Received in revised form 4 July 2017
Accepted 7 July 2017
Available online 4 August 2017
Editor: P. Shearer

Keywords:
coda interferometry
near-surface seismic anisotropy
Taiwan

ABSTRACT

We report the near-surface (<400 m) primary wave velocity (V_p), shear wave velocity (V_s), V_p/V_s ratio, Poisson's ratio and V_s anisotropy of Taiwan by applying seismic coda interferometry to 34 borehole-surface station pairs. We find clear characteristic $\cos 2\theta$ dependence of V_s in all the determinations, and about half of the amplitudes of anisotropy are larger than 10%, with the largest amplitudes up to 34%. The patterns of anisotropy fall into two categories, OPA (Orogeny-Parallel Anisotropy) and SAA (Stress-Aligned Anisotropy). Both types of anisotropy fit well the local geological fabrics and/or the ambient stress, and show strong correlation with the Poisson's ratios at the borehole sites. With these new findings and reported tomographic results, we infer that the SAA are likely confined to the uppermost portion of the crust, in particular to the fluid-saturated late-Quaternary deposits. The strong near-surface anisotropy also implies that delay times contributed by the shallow crust might have been underestimated in studies of shear-wave splitting measurements using the direct arrivals of earthquake waves.

1. Introduction

Seismic anisotropy of the Earth interior has been extensively studied in the past decades, ranging from the inner-core, core-mantle boundary, uppermost mantle to the crust, and the results have provided important constraints to the Earth structure, in complement to that provided by the variations of isotropic velocity (e.g., Montagner and Tanimoto, 1990; Tanimoto, 1991; Silver, 1996; Gung et al., 2003; Panning and Romanowicz, 2004; Deuss et al., 2010; Huang et al., 2015). Interestingly, but not surprisingly, the near-surface (~few hundred meters in depth) seismic anisotropy is much less explored because the commonly applied methods, such as the surface wave tomography, receiver functions and shear-wave splitting (SWS) measurement using earthquake data, do not have the adequate fine resolution for the near-surface seismic structure. Recently, it is reported that the near-surface seismic anisotropy can be well resolved by applying ambient noise tomography to a small area with dense seismic array (Lin et al., 2013), however, the array density required for the extraction of high frequency surface waves is a demanding task for larger scale applications.

In this study, we aim to better understand the near-surface seismic anisotropy of Taiwan. The island of Taiwan is located along the active arc-continent collision boundary between the Philippine Sea Plate (PSP) and the Eurasian Plate (EP), and is known for its tectonic complexities both in the subsurface plate interactions and mountain building processes between EP and PSP and the surface geological features (Fig. 1) (e.g., Angelier, 1990; Teng, 1996; Ho, 1997; Wu et al., 2014). There are several previous studies of anisotropy in Taiwan, either by SWS measurements using teleseismic events (Rau et al., 2000; Huang et al., 2006; Kuo-Chen et al., 2009) or by examining the azimuthal variations of P wave arrival times using active sources (Kuo-Chen et al., 2013), which have shown that the fast directions of the seismic anisotropy are generally parallel to the trend of the mountain belts, i.e., the orogeny-parallel direction. Besides, the anisotropy with fast directions perpendicular to the mountain belt, i.e., parallel to the maximum compressional stress, in the foreland of the mountain belt has been reported by SWS studies using local shallow (<40 km) earthquakes (Chang et al., 2009). Recently, the 3-D crustal models of V_s anisotropy, constructed from noise-derived surface waves, demonstrate that the orogeny-parallel anisotropy (OPA) is confined to the upper crust; nevertheless, the general distribution of the depth-integrated anisotropy over the crust remains the OPA pattern (Huang et al., 2015).

* Corresponding author.
E-mail address: ycgung@ntu.edu.tw (Y. Gung).

http://dx.doi.org/10.1016/j.epsl.2017.07.016
0012-821X/

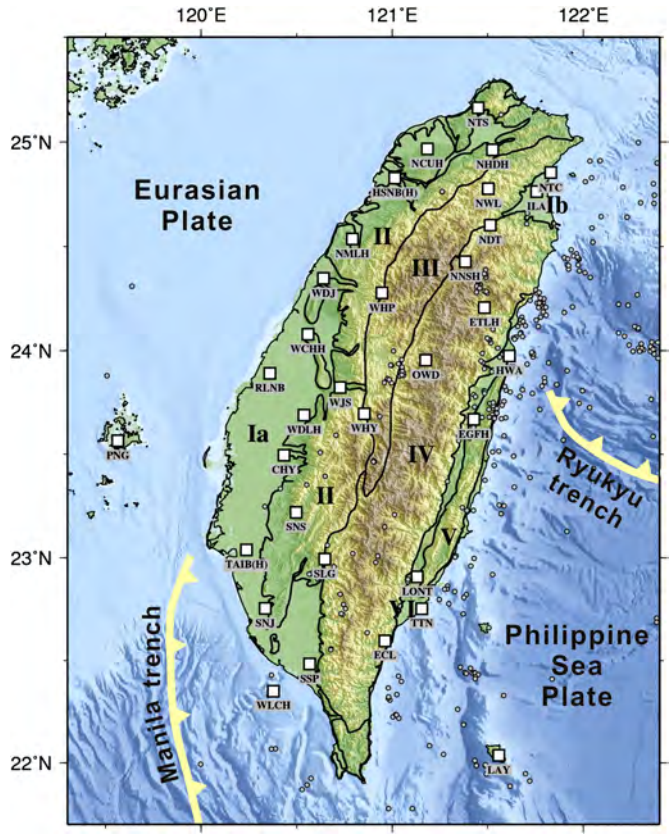

Fig. 1. The distribution of 34 borehole sites (open squares) and 398 local earthquakes (open circles) used in this study. The dark lines are boundaries of major tectonic units in Taiwan, and the indices shown in each geological unit are as follows: (I) Coastal Plains, including the Western Plain (Ia) and Ilan Plain (Ib), (II) Western Foothills, (III) Hsuehshan Range, (IV) Central Range, (V) Costal Range, and (VI) Longitudinal Valley.

While the above studies agree with the fact that the crustal anisotropy are closely linked to the main geological structures and the ambient stress field, none of them provide direct assessment to the near-surface anisotropy.

Taking advantage of the borehole seismic array recently (2011–) deployed by the Central Weather Bureau (CWB) of Taiwan and the Broadband Array in Taiwan for Seismology (BATS), we are able to apply the seismic interferometry technique to the vertical station pairs composed of the borehole and the overhead surface stations. In addition to V_s, the V_s azimuthal anisotropy can be obtained by examining the polarization of the vertically propagating shear waves using the extracted empirical Green's functions (EGFs) (e.g., Miyazawa et al., 2008; Lewis and Gerstoft, 2012; Nakata and Snieder, 2012).

In the following, we first briefly introduce the data and method. We then present the results of the measurements, including V_p, V_s, V_p/V_s ratio and V_s azimuthal anisotropy, and discuss their associations with local geology, ambient stress field, Poisson's ratio and the SWS studies. Finally, we summarize the major findings and implications of this study. Because the methods employed here have been well-established, we present details of the method and data processing in the supplementary material, where the validation and uncertainty estimates of the measurements are also provided.

2. Data and method

Data recorded by 34 island-wide borehole seismic stations deployed by CWB and BATS are used in this study (Fig. 1). Two strong motion sensors are equipped at each borehole site, with one on the surface and the other in the subsurface near the bottom of the borehole ranging from 100 to 400 m depth. Detailed station information is given in the supplementary material (Table S1).

2.1. Orientation correction of the borehole data

Accurate orientation in sensors of the station pairs is critical to the extraction of shear wave EGFs using seismic interferometry. Since the orientation of borehole sensors is usually not as reliable as the surface one, we examined the orientation of the borehole data using the surface orientation as a reference. This can be easily done because the largest amplitude of the cross-correlation function (CCF) of the borehole-surface station pairs appears when both orientations are consistent. The results show that the orientations are significantly biased in about half of the stations, which required corrections prior to the following data processing. Details of the data processing for CCFs and the correction procedure are given in the supplementary material.

2.2. Extraction of EGFs and measurement of azimuthal anisotropy

With the vertical borehole-surface station pairs, the EGFs for the structure in between can be extracted by cross-correlating either their continuous records or earthquake coda waves, or, by applying the de-convolution method to the earthquake signals recorded by both stations (e.g., Nakata and Snieder, 2012; Mehta et al., 2007). Since the borehole depths are rather shallow ($\lesssim$400 m), high frequency EGFs are preferred in order to accurately determine the V_s azimuthal dependence. Thus, the earthquake-based approaches, i.e., the de-convolution and coda cross-correlation methods, are considered in this study, as the high-frequency body waves in signals excited by the local earthquakes is much stronger than those in the ambient seismic noises.

We find that EGFs derived from the above two earthquake-based methods are fairly consistent in both the estimated isotropic velocities and the pattern of V_s azimuthal anisotropy. Since both methods are potentially sensitive to the incident angles of the earthquake waves, we have conducted a series of experiments to further assess the reliability of the resulting EGFs (supplementary material). The results indicate that EGFs extracted by the de-convolution method is more sensitive to the incident angles of earthquake waves, which is understandable, as the direct waves are used in this method. We also find that, the discrepancy between the estimated velocities by coda cross-correlation and those by the de-convolution method using events with near-vertical incident angles are very small ($\sim$2%). Accordingly, we employ the coda cross-correlation method to derive the EGFs of S waves and P waves in this study.

The coda waves of 398 local earthquakes with ML $>$ 4.0 (Fig. 1) during the time period from 2011 to 2014 are used to derive the high frequency (2–8 Hz) EGFs. To evaluate the V_s at any polarization directions, we first compute CCFs for the four combinations of horizontal components between the borehole and the surface stations, i.e., C_{NN}, C_{NE}, C_{EE}, and C_{EN}. The CCF for any given directions, θ, is then given by

$$C_{\theta\theta} = C_{NN}\cos\theta\cos\theta + C_{EN}\sin\theta\cos\theta + C_{NE}\sin\theta\cos\theta + C_{EE}\sin\theta\sin\theta, \quad (1)$$

where θ is the azimuth, i.e., angle measured clockwise from the north. The anisotropy property is estimated by using the following relationship (e.g., Alford, 1986), $V_s(\theta) = V_{iso} + V_{ani}\cos 2(\theta - \varphi)$, where V_{iso} is the isotropic V_s, V_{ani} the anisotropy coefficient, and φ is the fast polarization direction (FPD). We search for the optimal parameters, V_{iso}, V_{ani} and φ based upon the least-squared fitting criteria. Once the best-fitting parameters are located, the strength of anisotropy is defined by $(V_{fast} - V_{slow})/V_{fast}$, where V_{fast} and V_{slow} are V_s evaluated at the fast and slow polarization directions respectively.

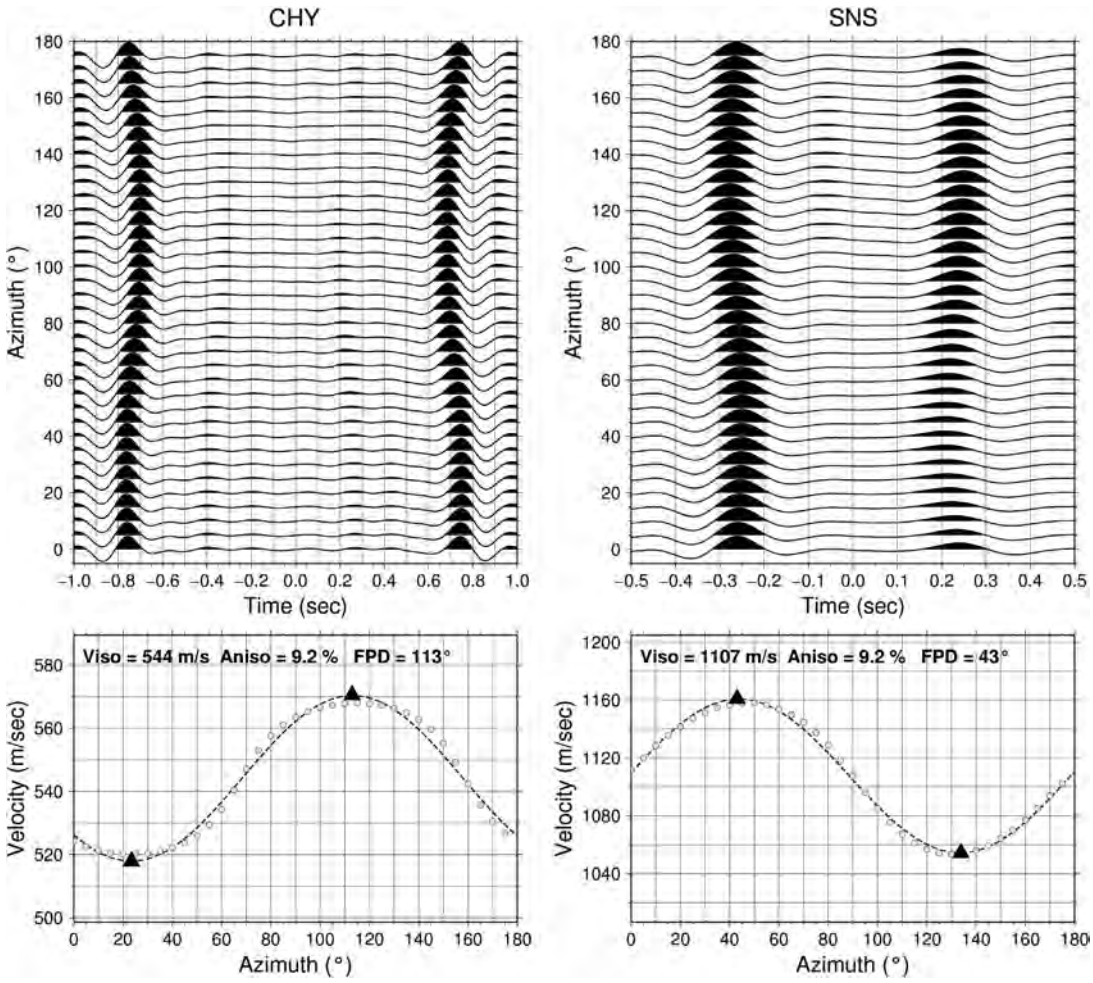

Fig. 2. Two examples of the anisotropy measurement at stations CHY and SNS. The top panels show the variations of EGF waveforms vs. polarization directions. The corresponding velocities, estimated by the peak arrivals, are marked by gray circles in the lower panels, and are best-fit by $V_s(\theta) = V_{iso} + V_{ani} \cos 2(\theta - \varphi)$, where V_{iso} is the isotropic V_s, φ is the fast polarization direction (FPD), and the strength of anisotropy is defined by $(V_{fast} - V_{slow})/V_{fast}$.

3. Results and discussions

Out of the 34 available borehole-surface station pairs, we have acquired 33 reliable determinations. Two examples are shown in Fig. 2, where the EGF waveforms at every 5° in azimuth are shown to illustrate the V_s variations with respect to the polarization directions of shear waves. Here the acausal part of EGFs is related to the up-going waves from the underlying borehole sensor to the surface, and is taken for the measurements, as they are stronger and more robust than the causal signals, which refers to the down-going waves from the surface side (supplementary material). It's worth mentioning that most of the observed V_s azimuthal dependences can be well fit by the characteristic $\cos 2\theta$ curves, as shown in the lower panels of Fig. 2. We have also presented results of all the other measurements in the supplementary material.

3.1. Isotropic velocities and V_p/V_s ratio

The lateral variations of seismic velocity are strong, ranging from ~300 m/s to ~2800 m/s for V_s and from ~1000 m/s to ~4800 m/s for V_p. The values of V_p/V_s ratio are also highly diverse, ranging from 1.46 to 4.5. The observed seismic velocity and V_p/V_s ratio correlate well with the surface geology (Fig. 3). The sites with lower seismic velocity and higher V_p/V_s are generally located in lowlands with unconsolidated fluid-saturated sediments, such as the Western Coastal Plain, Ilan Plain and Longitudinal Valley. While the sites with higher velocity, usually accompanied by lower V_p/V_s ratio, are generally distributed in the mountainous areas with metamorphic units.

3.2. V_s anisotropy

Likewise, the near-surface anisotropy exhibits a large variation in strength, with amplitudes ranging from 0.2% up to 34%, and both the strengths of anisotropy and distributions of the FPDs fit well with the local geology, i.e., the rock types and structural fabrics (e.g., Ho, 1997), and/or the ambient stress field (e.g., Chang et al., 2003). According to the corresponding mechanisms of anisotropy, these results could be generally categorized into two groups, the OPA and the SAA (Stress-Aligned Anisotropy). The OPA are referred to those with FPDs subparallel to the main trends of mountain ranges, i.e., the structural fabrics under mountain building processes, such as the foliation of the metamorphic rocks (e.g., Godfrey et al., 2000). The SAA are related to the opening of fluid-filled micro-fractures in sediments subject to the lateral compression and extension (e.g., Crampin, 1994). As a result, the FPDs of SAA are subparallel to the directions of maximum compression stresses, which are approximately in line with the convergence direction between the PSP and the EP and perpendicular to the mountain trends.

About one third of the total results are classified into the OPA group (Fig. 4a), and most of them are located in the mountainous areas including the Central Range, Hsuehshan Range and Western Foothills. The measured FPDs are clearly related and subpar-

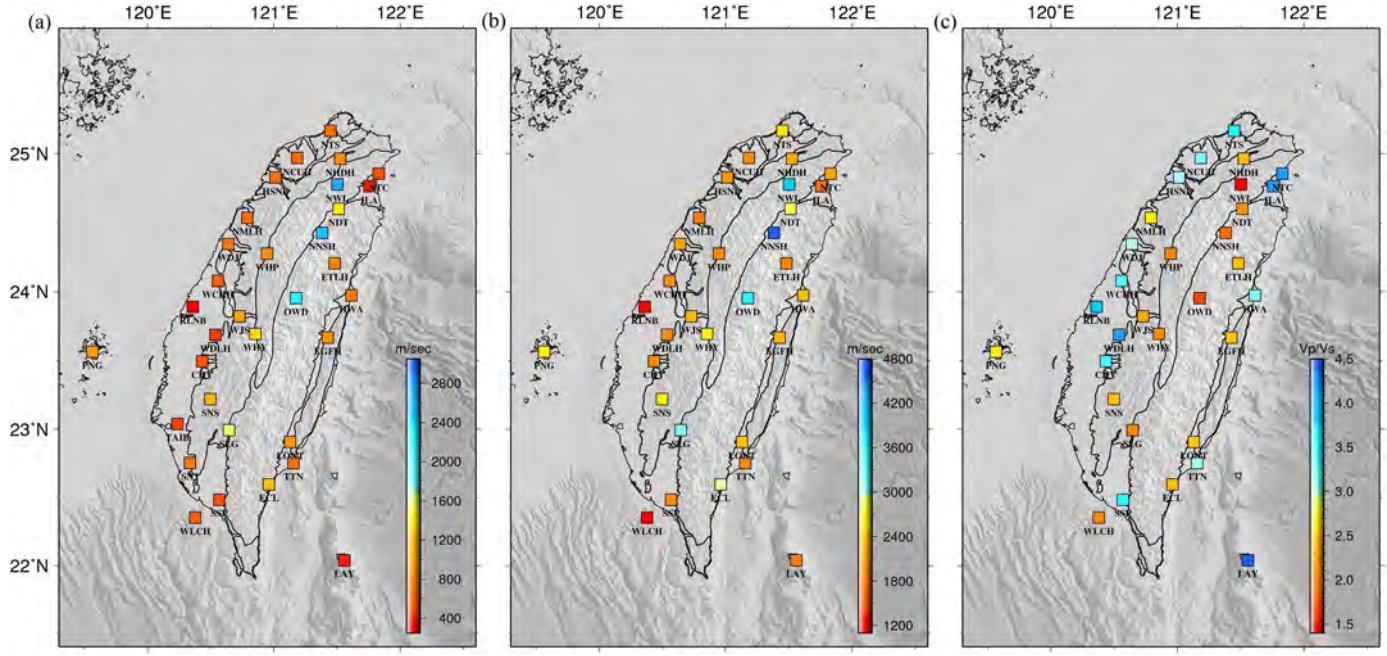

Fig. 3. Results of measurements of near-surface seismic velocity from borehole stations in Taiwan. The isotropic V_s at each station are shown in panel a; the V_p at each station are shown in panel b; the V_p/V_s ratio at each station are shown in panel c.

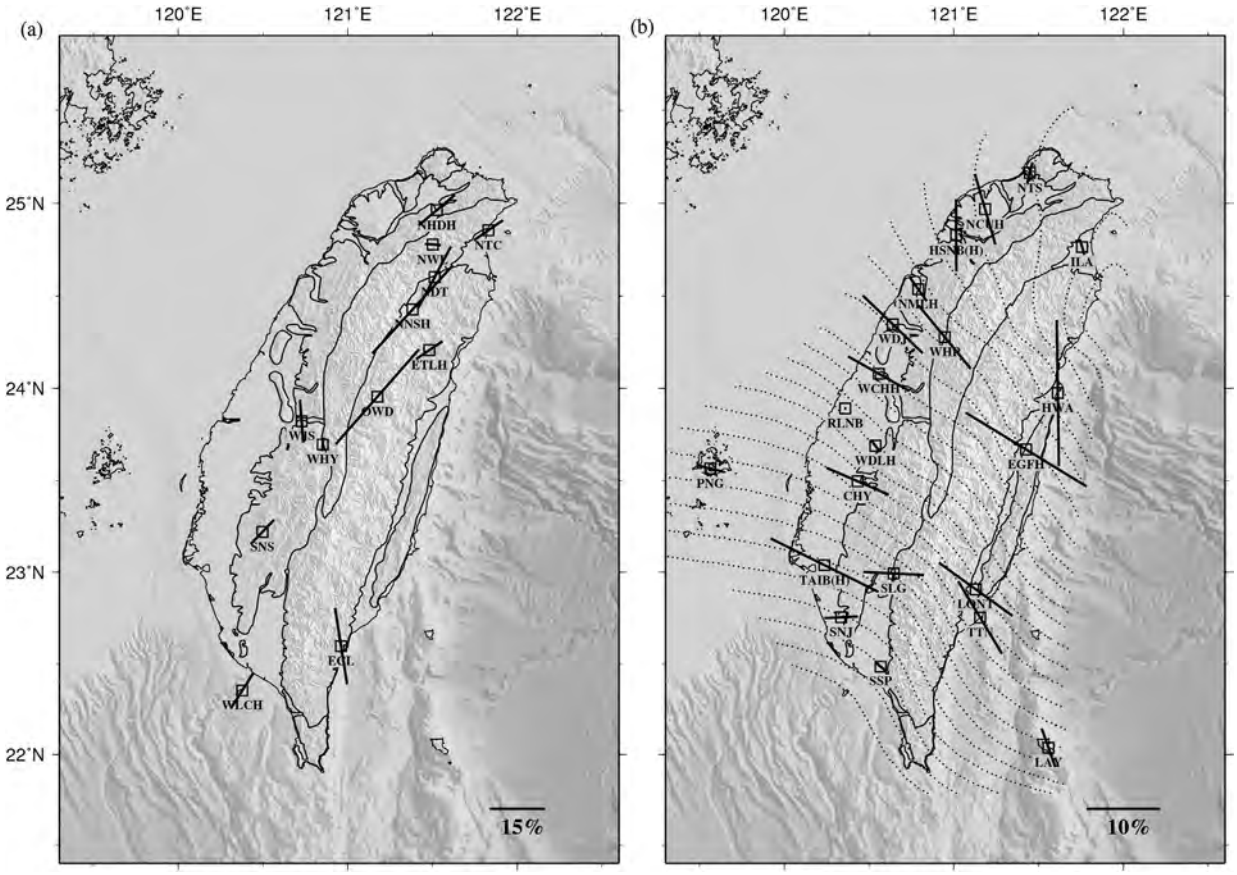

Fig. 4. Results of measurements of near-surface seismic anisotropy from borehole stations in Taiwan. The V_s azimuthal anisotropy with FPD subparallel the main trains of mountain ranges are shown in panel a, and those with FPD subparallel to the maximum compression stress trajectories, indicated by dashed lines, as adopted from Chang et al. (2003), are shown in panel b.

allel to the dominant fabric orientations of the local bedrocks (Ho, 1997). The largest amplitudes of anisotropy are observed at the two stations in the slate belt of the Central Ranges, stations OWD (34%) and NNSH (32.6%), where the slaty cleavages appear to provide significant contribution. The well depths in both sites are about 290 m, and the rocks in the well are mainly composed of slate, with cleavages trending in ∼N20°E and ∼N35°E, respectively, fairly consistent with the measured FPDs in both sites, which are N41°E at OWD, and N42°E at NNSH, respectively. The observations demonstrate that the fabrics of slate cleavages are capable of generating strong elastic anisotropy. A much smaller amplitude of anisotropy (8.7%) is observed at the station ETLH, which is also located in the Central Range. While the regional rock formations are composed of the green schist of the Mesozoic Tananao complex with cleavages trending in ∼N30°E, the weaker anisotropy at ETLH is understandable, as the upper half (65 m) of the well body is covered by alluvial gravels and sands, which likely significantly reduce the OPA strength. OPA are observed in the Western Foothills as well, for instance, at the station NHDH and SNS, where the amplitudes of anisotropy are relatively weak at 12.9% and 9.2%, respectively. We argue that the OPA are mainly attributed to the regular bedding plane of the bedrocks in the above two sites, which is composed of the intercalations of sandstones and shale, with trends of bedding plane in ∼N50°E/30E at NHDH and ∼N60°E/60E at SNS.

Note that none of the OPA sites appear in the coastal plains, and none of the SAA sites are located in the mountain ranges either. The sites with SAA are distributed in the coastal plain, and the Longitudinal Valley, with few in the Western Foothills, as displayed in Fig. 4b, where the maximum compression stress trajectories, as adopted from Chang et al. (2003), are also shown for comparison. According to the reported well log data and the 1:50000 geological maps from Central Geological Survey, the sites with SAA are generally covered by unconsolidated alluvium or poorly consolidated sedimentary layers, consistent with the favor structures of the proposed SAA mechanism (e,g., Crampin, 1994; Crampin and Gao, 2010).

The weakest SAA is observed at RLNB (0.2%), while the strongest ones are at HWA (19.9%) and EGFH (19.3%). At the Western Coastal Plain, the V_S at RLNB, 288 m/s, is also the lowest among all the results. The borehole depth at RLNB is 100 m, and the well body is covered by late Quaternary alluvial deposits, which are mainly composed of unconsolidated mud, fine-grained sand and gravels. The small anisotropy might be attributed to the fact that fractures are still premature in the young sediments. On the other hand, regardless the weak anisotropy, the FPD at RLNB is fairly resolved (∼E–W) and fits well with the directions of the local maximum compression stress. Both HWA and EGFH are located in alluvial deposits of the Longitudinal Valley, the active plate suture between the colliding PSP and EP. The borehole depth at HWA is 289 m, and the station was drilled into the alluvial deposits, composed by unconsolidated gravels, sand, and mud layers. The SAA amplitudes in the northern Longitudinal Valley are apparently stronger than those in the western Taiwan, where the typical SAA amplitudes are less or about 10%, and this is likely related to the greater strain rates in the plate boundary of the Longitudinal Valley (Chang et al., 2003).

3.3. Types of anisotropy and Poisson's ratio

In Fig. 5, we compare types of anisotropy with two important properties of seismic velocity, V_p/V_s ratio and Poisson's ratio. In general, as compared to the OPA sites, the SAA sites are usually characterized by smaller V_s and larger V_p/V_s (Fig. 5a).

The velocity ratio can be easily converted to Poisson's ratio (σ), defined by $[(V_p/V_s)^2-2]/[2(V_p/V_s)^2-2]$, which is widely

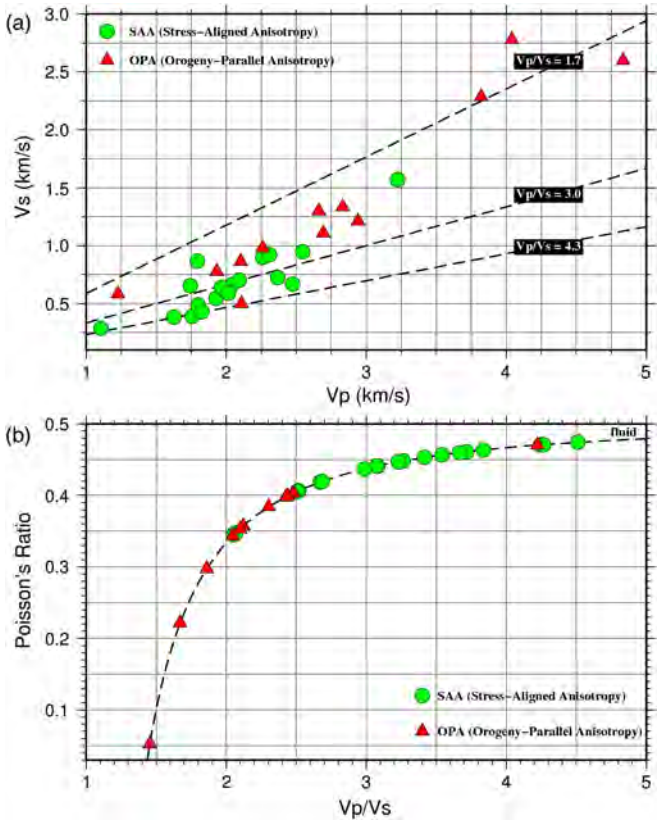

Fig. 5. (a) Comparison of near-surface V_p and isotropic V_s measurements at each borehole site. The red triangles and the green circles show the different anisotropy categories of our results, the OPA and the SAA; the V_p/V_s ratio of 1.7, 3.0 and 4.3 are shown by dash lines. (b) Poisson's ratio versus velocity ratio. The red triangles and the green circles show the different anisotropy categories of our results, the OPA and the SAA; the dash curve shows the relation between velocity ratio and Poisson's ratio. (For interpretation of the references to color in this figure legend, the reader is referred to the web version of this article.)

used in petroleum industry to discriminate different types of rock and presence of fluid or gas. According to the laboratory measurements of various rock specimens, the Poisson's ratios fall into the range from 0.2 to 0.4 for most rock samples. While for highly fluid-saturated marine sediments, the Poisson's ratios vary from above 0.49 at the sea floor to 0.41 at the depth of 1000 m (e.g., Hamilton, 1979). The distinction between SAA and OPA is clearly shown in their corresponding Poisson's ratio (Fig. 5b). In contrast to the OPA sites, the Poisson's ratio observed in most SAA sites are larger than 0.4, indicating that the micro-fractures in near-surface sediments are likely fluid-saturated, consistent with the fluid-filled property of extensive-dilatancy anisotropy (e.g., Crampin, 1987, 1994). It is worth mentioning that the highest Poisson's ratio is observed at ILA station and the well log data report indicates that there are lots of water inflows in the ILA borehole site.

3.4. Estimated shear-wave splitting times

We estimate the expected splitting times of shear waves at each borehole site, assuming the same seismic structures, V_s and V_s anisotropy, extend down to 1 km in depth. The results are shown in Fig. 6, where the median 0.24 s is used as the reference scale.

We also compare estimated delay times with other crustal SWS results (Chang et al., 2009 and Okaya et al., 2016) nearby each borehole site within a radius of 10 km, shown in Fig. 7. Most of the expected delay times are similar to the crustal SWS measurements, and the comparison implies that the delay times induced by the near-surface anisotropy are much larger than generally assumed, particular at sites with low V_s.

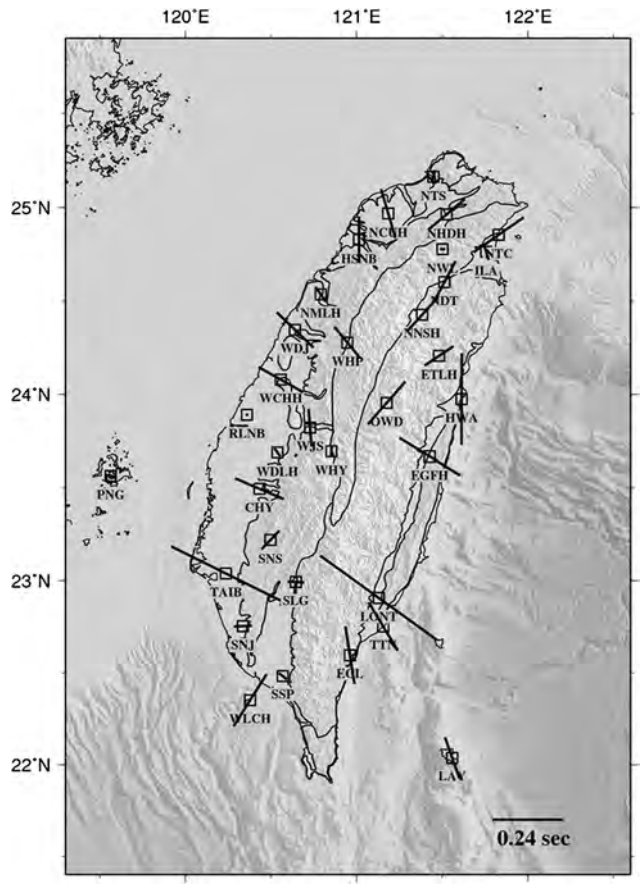

Fig. 6. Estimated delay times of shear wave splitting (SWS) induced by the near-surface anisotropy at each borehole site, assuming the same seismic structures as those shown in Fig. 4 extend to 1 km in depth. The median of all the results, 0.24 s is used as the reference scale.

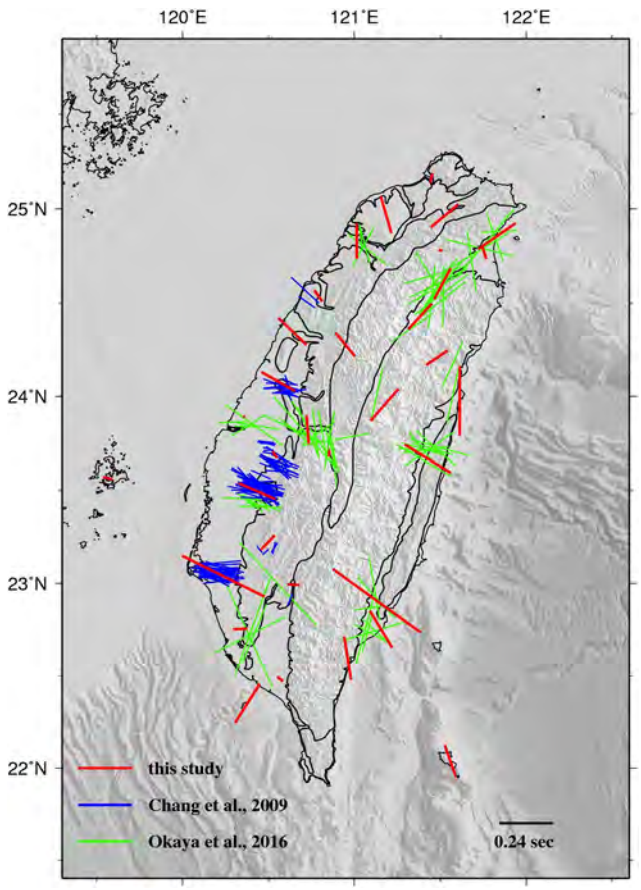

Fig. 7. Comparison of our estimated delay times (same as Fig. 6) and other crustal SWS results nearby each borehole site. The results of our study, Chang et al. (2009) and Okaya et al. (2016) are marked as red, blue and green, separately. (For interpretation of the references to color in this figure legend, the reader is referred to the web version of this article.)

4. Summary

Results of this study have provided robust constraints to the near-surface seismic structure of Taiwan. In accord with the varied surface geology covering different terrains in the Taiwan mountain belt, the observed V_p, V_s and the V_s azimuthal anisotropy demonstrate very large lateral variations, much stronger than those reported in the tomographic models of Taiwan (e.g., Wu et al., 2007; Huang et al., 2015).

According to the origins and mechanisms of anisotropy, the observed patterns of anisotropy fall into two categories, SAA and OPA, which seemingly fit well either the local geological fabrics or the regional tectonic ambient stress at the borehole sites. The SAA are widely distributed in the Western Coastal Plains and the northern Western Foothills and the OPA results are located in the Central Range, Hsuehshan Range and Western Foothills; both patterns are closely related to Poisson's ratio and consistent with the SWS measurements using local shallow earthquakes (Chang et al., 2009 and Okaya et al., 2016). However, SAA anisotropy is not present in the upper crust (<10 km) of the crustal model of V_s anisotropy constructed by the noise-derived Rayleigh waves (Huang et al., 2015), suggesting that the SAA is probably confined to the uppermost crust (<3 km), beyond the effective sensitivity of the broad-band Rayleigh waves (4–20 s) used in the modeling of Huang et al. (2015).

The strong near-surface anisotropy reported here also bring new insights into the interpretation of SWS studies. It has been pointed out that the fast direction of SWS is more sensitive to shallow anisotropy structure (e.g., Rümpker and Silver, 1998), and our results further suggest that the very shallow part of the crust, particularly near-surface geology, may have a significant contribution to the shear wave splitting times, which are usually underestimated in the studies of SWS measurement using high frequency direct arrivals of earthquake waves.

Acknowledgements

This work was supported by the Ministry of Science and Technology of Taiwan (MOST 105-2116-M-002-005-). The seismic data were essential for this study. The authors would like to thank the Broad-Band Array in Taiwan for Seismology (BATS) and Central Weather Bureau Broad-Band array (CWBBB) for providing data used in this study.

Appendix A. Supplementary material

Supplementary material related to this article can be found online at http://dx.doi.org/10.1016/j.epsl.2017.07.016.

References

Alford, R.M., 1986. Shear data in the presence of azimuthal anisotropy: Dilley, Texas. SEG Technical Program Expanded Abstracts, pp. 476–479.

Angelier, J., 1990. Foreword, special issue 'Geodynamic evolution of the Eastern Eurasian margin'. Tectonophysics 183, VII–X.

Chang, C.-P., Chang, T.-Y., Angelier, J., Kao, H., Lee, J.-C., Yu, S.-B., 2003. Strain and stress field in Taiwan oblique convergent system: constraints from GPS observation and tectonic data. Earth Planet. Sci. Lett. 214 (1), 115–127.

Chang, E.T., Liang, W.-T., Tsai, Y.-B., 2009. Seismic shear wave splitting in upper crust characterized by Taiwan tectonic convergence. Geophys. J. Int. 177 (3), 1256–1264.

Crampin, S., 1987. Geological and industrial implications of extensive-dilatancy anisotropy. Nature 328, 491–496.

Crampin, S., 1994. The fracture criticality of crustal rocks. Geophys. J. Int. 118 (2), 428–438.

Crampin, S., Gao, Y., 2010. A review of the new understanding of fluid-rock deformation in the crack-critical Earth. Rock Stress Earthq., 235.

Godfrey, N.J., Christensen, N.I., Okaya, D.A., 2000. Anisotropy of schists: contribution of crustal anisotropy to active source seismic experiments and shear wave splitting observations. J. Geophys. Res., Solid Earth (1978–2012) 105 (B12), 27991–28007.

Deuss, A., Irving, J.C., Woodhouse, J.H., 2010. Regional variation of inner core anisotropy from seismic normal mode observations. Science 328 (5981), 1018–1020.

Gung, Y., Panning, M., Romanowicz, B., 2003. Global anisotropy and the thickness of continents. Nature 422, 707–711. http://dx.doi.org/10.1038/nature01559.

Hamilton, E.L., 1979. V_p/V_s and Poisson's ratios in marine sediments and rocks. J. Acoust. Soc. Am. 66 (4), 1093–1101.

Ho, C.-S., 1997. An Introduction to the Geology of Taiwan, Explanatory Text of the Geologic Map of Taiwan, second ed. Central Geological Survey, Ministry of Economic Affairs, Taipei. 164 pp.

Huang, B.S., Huang, W.G., Liang, W.T., Rau, R.J., Hirata, N., 2006. Anisotropy beneath an active collision orogen of Taiwan: results from across islands array observations. Geophys. Res. Lett. 33 (24).

Huang, T.-Y., Gung, Y., Kuo, B.-Y., Chiao, L.-Y., Chen, Y.-N., 2015. Layered deformation in the Taiwan orogen. Science 349 (6249), 720–723. http://dx.doi.org/10.1126/science.aab187.

Kuo-Chen, H., Wu, F.T., Okaya, D., Huang, B.S., Liang, W.T., 2009. SKS/SKKS splitting and Taiwan orogeny. Geophys. Res. Lett. 36 (12).

Kuo-Chen, H., Środa, P., Wu, F., Wang, C.Y., Kuo, Y.W., 2013. Seismic anisotropy of the upper crust in the mountain ranges of Taiwan from the TAIGER explosion experiment. Terr. Atmos. Ocean. Sci. 24 (6), 963–970.

Lewis, M.A., Gerstoft, P., 2012. Shear wave anisotropy from cross-correlation of seismic noise in the Parkfield pilot hole. Geophys. J. Int. 188 (2), 626–630.

Lin, F.-C., Li, D., Clayton, R.W., Hollis, D., 2013. High-resolution 3D shallow crustal structure in Long Beach, California: application of ambient noise tomography on a dense seismic array. Geophysics 78 (4), Q45–Q56. http://dx.doi.org/10.1190/geo2012-0453.1.

Miyazawa, M., Snieder, R., Venkataraman, A., 2008. Application of seismic interferometry to extract P- and S-wave propagation and observation of shear-wave splitting from noise data at Cold Lake, Alberta, Canada. Geophysics 73 (4), D35–D40.

Montagner, J.-P., Tanimoto, T., 1990. Global anisotropy in the upper mantle inferred from the regionalization of phase velocities. J. Geophys. Res., Solid Earth (1978–2012) 95 (B4), 4797–4819.

Mehta, K., Snieder, R., Graizer, V., 2007. Downhole receiver function: a case study. Bull. Seismol. Soc. Am. 97 (5), 1396–1403.

Nakata, N., Snieder, R., 2012. Estimating near-surface shear wave velocities in Japan by applying seismic interferometry to KiK-net data. J. Geophys. Res., Solid Earth (1978–2012) 117 (B1).

Okaya, D., Christensen, N.I., Ross, Z.E., Wu, F.T., 2016. Terrane-controlled crustal shear wave splitting in Taiwan. Geophys. Res. Lett. 43 (2), 556–563.

Panning, M., Romanowicz, B., 2004. Inferences on flow at the base of Earth's mantle based on seismic anisotropy. Science 303 (5656), 351–353.

Rau, R.-J., Liang, W.-T., Kao, H., Huang, B.-S., 2000. Shear wave anisotropy beneath the Taiwan orogen. Earth Planet. Sci. Lett. 177 (3), 177–192.

Rümpker, G., Silver, P.G., 1998. Apparent shear-wave splitting parameters in the presence of vertically varying anisotropy. Geophys. J. Int. 135, 790–800.

Silver, P.G., 1996. Seismic anisotropy beneath the continents: probing the depths of geology. Annu. Rev. Earth Planet. Sci. 24, 385–432.

Tanimoto, T., 1991. Global upper mantle tomography of seismic velocities and anisotropies. J. Geophys. Res. 96 (B12), 20–337.

Teng, L.S., 1996. Extensional collapse of the northern Taiwan mountain belt. Geology 24 (10), 949–952.

Wu, Y.-M., Chang, C.-H., Zhao, L., Shyu, J.B.H., Chen, Y.-G., Sieh, K., Avouac, J.P., 2007. Seismic tomography of Taiwan: Improved constraints from a dense network of strong motion stations. J. Geophys. Res., Solid Earth. (1978–2012) 112(B8).

Wu, F.T., Kuo-Chen, H., McIntosh, K.D., 2014. Subsurface imaging, TAIGER experiments and tectonic models of Taiwan. J. Asian Earth Sci. 90, 173–208.